

EXPERIMENTAL AND COMPUTATIONAL ANALYSIS OF STEAM CONDENSATION IN THE PRESENCE OF AIR AND HELIUM

MATTEO BUCCI,^{a*} WALTER AMBROSINI,^b and NICOLA FORGIONE^b

^a*Cea Saclay, CEA/DEN/DANS/DM2S/STMF/LATF
91191 Gif-sur-Yvette Cedex, France*

^b*Università di Pisa, Largo Lucio Lazzarino 2, 56126 Pisa, Italy*

This paper discusses the results of investigations devoted to the study of steam condensation in the presence of air and a light noncondensable gas. A double strategy has been adopted, including complementary experimental and computational activities. Novel data have been made available by the CONAN (CONDensation with Aerosols and Noncondensable gases) facility, investigating the effects induced by light noncondensable gases in ex-

perimental configurations that were scarcely investigated in past studies. Computational fluid dynamics condensation models have been developed and validated. The suitability of helium as a substitute for hydrogen in experimental activities has been investigated by theoretical and computational analyses that allow establishing simple criteria for the scaling of condensation tests in the presence of a light noncondensable gas.

I. INTRODUCTION

Condensation in the presence of noncondensable gases has a well-known relevance in nuclear safety analyses since it represents an important heat sink for removing the energy released by the discharge of the primary water during a postulated loss-of-coolant accident. Nevertheless, it could strongly affect containment atmosphere mixing, influencing the distribution of hydrogen and other noncondensable gases hypothetically delivered in severe accident conditions.

Condensation in the presence of light noncondensable gases is therefore of primary relevance in safety analyses of the containment system, for which an in-depth understanding is desirable.

In the past decades, the phenomenon has been investigated from the theoretical and the experimental points of view, and extensive databases were made available by both integral and separate-effects test facilities.^{1–13} However, the need for producing new experimental data has recently emerged to promote the validation of computa-

tional fluid dynamics (CFD) codes in view of their application to containment safety analyses.

One of the most important activities carried out in the field of condensation modeling in the last decades is probably International Standard Problem 47 (ISP47) (Ref. 13). Analyzing the results of this benchmark exercise, researchers recognized a general need for achieving a better understanding of the effect of light noncondensable gases and improving the predictive capabilities of CFD models. For this purpose, smaller-scale experimental analyses are advisable over those used for ISP47. In this direction, research activities^{14,15} in the field of condensation modeling have been coordinated by University of Pisa and Commissariat à l'Energie Atomique in the frame of the SARnet network on severe accidents (www.sar-net.eu). The separate-effects CONAN (CONDensation with Aerosols and Noncondensable gases) facility operated by University of Pisa has been modified and adopted to produce data on steam condensation in an atmosphere of air and helium.^{16–18} Computational tools have been developed having multiple purposes. On one hand, mechanistic models based on the principles of gas diffusion in the

boundary layer have been developed and applied mainly to the analysis of small-scale separate-effects condensation tests.^{19–22} These models, hardly applicable to large-scale domain analyses, are however useful in significantly improving the understanding of physical phenomena involved in the condensation process. On the other hand, other models have been purposely conceived for the analysis of large-scale facilities or full-scale containment. These models have been developed based on the heat and mass transfer analogy.^{23–25}

The aim of this paper is to summarize the main findings of these computational and experimental investigations, focusing on those aspects that can constitute the basis for further improvements in the understanding of condensation phenomena. The CFD tools developed in this research activity are first illustrated. Then, the results of experimental campaigns and the prediction of CFD tools are discussed. Finally, the suitability of helium as a substitute for hydrogen in experimental activities is investigated.

II. CFD MODELS

The set of balance equations characterizing the behavior of a multicomponent mixture of steam, air, and helium is given by the mixture continuity equation, species balance equations for two of the three species (air and helium in our case), the momentum balance equation, and the thermodynamic energy balance equation (see Nomenclature on p. 130):

mixture continuity:

$$\frac{\partial \rho}{\partial t} + \nabla \cdot (\rho \mathbf{u}) = S_m ; \quad (1)$$

air species conservation:

$$\frac{\partial \rho_a}{\partial t} + \nabla \cdot (\rho_a \mathbf{u}) = -\nabla \cdot \mathbf{j}_a ; \quad (2)$$

helium species conservation:

$$\frac{\partial \rho_{he}}{\partial t} + \nabla \cdot (\rho_{he} \mathbf{u}) = -\nabla \cdot \mathbf{j}_{he} ; \quad (3)$$

momentum:

$$\frac{\partial \rho \mathbf{u}}{\partial t} + \nabla \cdot (\rho \mathbf{u} \mathbf{u}) = \nabla \cdot \boldsymbol{\tau} - \nabla P + \rho \mathbf{g} + \mathbf{S}_q ; \quad (4)$$

thermodynamic energy:

$$\frac{\partial \rho e}{\partial t} + \nabla \cdot (\rho \mathbf{u} h) = \nabla \cdot \left(k \nabla T - \sum_{k=v,a,he} \mathbf{j}_k h_k \right) + S_h . \quad (5)$$

A common approach for modeling wall condensation in CFD codes consists of assigning the volumetric source terms appearing in the mass and species balance equations only to cells adjacent to the condensing interface.¹⁴ These source terms are linked to the mixture continuity equation, the steam balance equation, and the momentum and the energy balance equations (see Fig. 1). Volumetric sources of mass (steam), energy, and momentum are therefore linked in the balance equations, defined as

$$\begin{aligned} S_m &= \dot{m}''_{v,i} / 2\Delta c , \\ S_h &= S_m h_{v,i} , \\ \text{and} \\ \mathbf{S}_q &= S_m \mathbf{u}_c , \end{aligned} \quad (6)$$

where

$2\Delta c$ = thickness of the cell

$h_{v,i}$ = steam enthalpy at the temperature of the condensing interface

\mathbf{u}_c = mixture velocity in the center of the cell close to the interface where the source term is applied.

The heat transfer through the condensing plate is modeled by a conjugated heat transfer approach, obtained by assigning an appropriate source term to the solid cells contiguous to the condensing interface:

$$S_{h,p} = -S_m h_{lv,i} , \quad (7)$$

where $h_{lv,i}$ is the steam latent heat. In order to evaluate the condensation mass flux and thus the sources, different

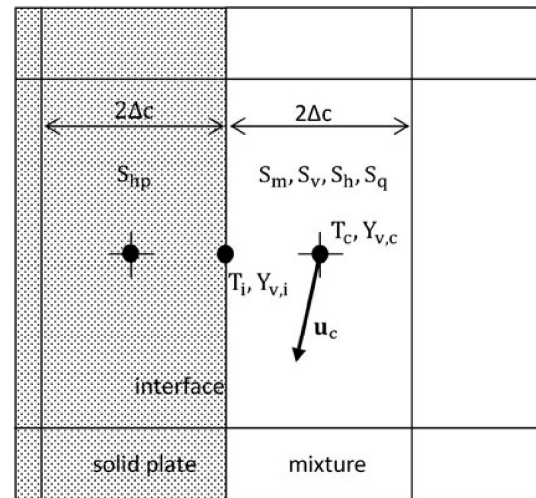


Fig. 1. Sketch of the discretization in the near-wall condensing plate region.

models have been developed adopting different strategies and having different purposes. A brief description of them is given in Secs. II.A and II.B.

II.A. HMTDM Diffusion-Based Method

HMTDM (Heat and Mass Transfer Diffusion-based Model) is capable of evaluating the mass transfer rates on the basis of concentration distributions in the near-wall region, without requiring any additional specific closure law; however, it requires a very fine space meshing since its accuracy depends on that of the concentration profiles next to the condensing wall. The condensation mass flux is calculated as

$$\dot{m}_{v,i}'' = \frac{\mathbf{j}_{v,i} \cdot \mathbf{n}_i}{1 - Y_{v,i}} , \quad (8)$$

where \mathbf{n}_i is the normal to the condensing interface, pointing toward the fluid domain. The mechanistic character of the model consists of the way in which the diffusion fluxes are calculated. In this aim, two different models can be adapted: the effective binary diffusivity approximation model (EBD) and the full multispecies mass transfer model (MSD).

Here and in the following, the assumption is made that the condensate film is very thin and then that its thermal resistance is negligible with respect to the overall heat transfer resistance. The interface is therefore identified with the condensing wall surface.

Commercial CFD codes often make use of the so-called EBD approximation. The diffusion mass flux of a species is given by

$$\mathbf{j}_k = -\rho(D_{km} + D_t)\nabla Y_k , \quad (9)$$

where

D_{km} = equivalent binary molecular diffusivity of the species k in the mixture

D_t = turbulent diffusivity, estimated according to the selected turbulence model.

In CFD codes, like FLUENT (Ref. 26), the equivalent binary diffusivity can be estimated by

$$D_{km} = \frac{1 - X_k}{\sum_{j \neq k} X_j / D_{kj}} . \quad (10)$$

As shown in a forthcoming work,²⁷ this formulation gives an appropriate description of diffusion for the condensable species but not for noncondensable gases. Nevertheless, it is remarked that in general, this formulation implies

$$\sum_{k=1}^n -\rho D_{km} \nabla Y_k = \sum_{k=1}^n \mathbf{j}_k \neq 0 . \quad (11)$$

A systematic error is therefore introduced in the balance equations of noncondensable species and, in particular, for the species for which the balance equation is not solved (being obtained summing the continuity equation and the balance equations of the other species). Indeed, when the details of molecular transport are dominant, as in the condensation boundary layer, the EBD approximation can lack in accuracy.

Overcoming these difficulties requires an appropriate model that can be deduced based on the principles of irreversible thermodynamics, as shown by Bucci,¹⁸ or based on the kinetic theory of gases, as shown by Taylor and Krishna.²⁸ The diffusion mass flux of the generic k 'th species in a mixture of n species is given by

$$\mathbf{j}_k = -\rho \sum_{j=1}^{n-1} (\mathcal{D}_{kj} + D_t) \nabla Y_j , \quad (12)$$

where \mathcal{D}_{kj} are the terms of the multispecies diffusion matrix $[\mathbf{D}]$, given by

$$[\mathbf{D}] = [\mathbf{A}]^{-1} [\mathbf{R}] \quad (13)$$

with

$$\mathcal{A}_{kk} = -M \left(\frac{X_k}{D_{km} M_n} + \sum_{j \neq k}^n \frac{X_j}{D_{kj} M_j} \right) ,$$

$$\mathcal{A}_{kj} = X_k M \left(\frac{1}{D_{kj} M_j} - \frac{1}{D_{kn} M_n} \right) ,$$

$$\mathcal{R}_{kk} = M \left(\frac{X_k}{M_n} + \frac{1 - X_k}{M_k} \right) ,$$

and

$$\mathcal{R}_{kj} = X_k M \left(\frac{1}{M_j} + \frac{1}{M_n} \right) . \quad (14)$$

Because of its computational cost, HMTDM (mostly MSD) is hardly applicable to large-scale geometries. However, it is a very useful tool for achieving a better understanding of the physical phenomena involved in condensation and relevant information for the development of coarser models for large-scale analyses.

II.B. HMTAM (Analogy-Based Method)

HMTAM (Heat and Mass Transfer Analogy-based Model) estimates the condensation mass transfer rates on the basis of the heat and mass transfer analogy. The condensation mass flux is assigned as

$$\dot{m}_{v,i}'' = h_m \frac{Y_{v,i} - Y_{v,b}}{1 - Y_{v,i}} = h_m B_m , \quad (15)$$

where

h_m = mass transfer coefficient

B_m = condensation driving force.

The mass transfer coefficient includes two terms,

$$h_m = h_{m,0} F, \quad (16)$$

which are the mass transfer coefficient at low mass transfer rates $h_{m,0}$ deduced on the basis of the heat and mass transfer analogy, and the correction factor of Stefan F (Ref. 29) aimed at accounting for suction effects. Based on the heat and mass transfer analogy, for low mass transfer rates, we give the Sherwood number by

$$Sh_{0,x} = Nu_{0,x} (Sc/Pr)^{1/3}, \quad (17)$$

and the corresponding local mass transfer coefficient by

$$h_{m,0} = Sh_{0,x} \frac{\rho D_{vm}}{x}. \quad (18)$$

The condensation mass flux is therefore given by

$$\dot{m}''_{v,i} = h_{m,0} F \frac{Y_{v,i} - Y_{v,b}}{1 - Y_{v,i}} = Sh_{0,x} \frac{\rho D_{vm}}{x} \ln \frac{Y_{nc,b}}{Y_{nc,i}}. \quad (19)$$

The key point of the model is the choice of the appropriate correlation for the Nusselt number, which can be troublesome for complex geometries and not well defined phenomenologically. On one hand, the Schlichting correlation³⁰ can be adopted for forced convection turbulent boundary layers on flat plates:

$$Sh_{0,x,FC} = 0.0296 Re_x^{0.8} Sc^{1/3}. \quad (20)$$

On the other hand, in natural convection boundary layers, the McAdams correlation³¹ can be used:

$$Sh_{0,x,NC} = 0.13 Gr_x^{1/3} Sc^{1/3}. \quad (21)$$

To deal with mixed convection effects, according to Incropera,³¹ we estimate the Sherwood number as

$$Sh_{0,x,MC}^n = |Sh_{0,x,FC}^n \pm Sh_{0,x,NC}^n|, \quad (22)$$

where n is taken equal to 3. The plus sign (+) is used in buoyancy-opposed conditions (gravity and inertia terms have different directions), whereas the minus sign (−) should be used in buoyancy-aided conditions whenever turbulent flows with possible laminarization effects are addressed.²⁵ Despite the difficulties associated with the choice of appropriate correlation, since the use of relatively coarse meshing is possible, a significant reduction

of computational resources is achieved, making this model applicable to large-scale or even to full-containment-scale analyses.

II.C. Modeling of Turbulence Effects

The renormalization group (RNG) $\kappa - \varepsilon$ model is here used to account for turbulence effects with both condensation models. Anyway, a different approach is used to deal with the near-wall turbulence. On one hand, the HMTDMs require a very fine meshing in the region near the condensing wall since the accuracy of the condensation models relies on the capability to estimate temperature and concentration gradients in the condensing boundary layer. For this reason, appropriate low Reynolds functions are adopted, which are referred to as enhanced wall treatment (EWT) in the FLUENT code.²⁶ On the other hand, HMTAM allows adopting a relatively coarse discretization in the near-wall region. Standard logarithmic wall functions are thus used, even if not purposely conceived to deal with transpiring boundary layers. Despite the use of the RNG $\kappa - \varepsilon$ model, other choices are possible. The authors investigated different options and concluded that most turbulence models with low Reynolds capabilities are able to describe the qualitative behavior of transpiring boundary layers.^{18,19} The use of low Reynolds functions (for HMTDM) or the standard wall functions (for HMTAM) is legitimated by the experimental observation that a continuous liquid film on the surface is unlikely (see Sec. III.C). Whenever a continuous liquid film is present, the accuracy of these approaches should be addressed.

III. THE CONAN FACILITY

The CONAN facility is operated by the Department of Mechanical, Nuclear and Production Engineering of the University of Pisa. The apparatus was conceived to collect data of steam condensation of interest for nuclear reactor containment thermal-hydraulic analysis. The facility consists of three different loops (primary, secondary, and tertiary), which accomplish the operating needs encountered in running the experiments (see Fig. 2):

1. In the primary loop, the mixture of steam and noncondensable gases circulates and partly condenses on a flat wall.
2. The secondary loop provides the required cooling of the condensing plate by circulating water in a rear channel, whose temperature and flow rate can be varied.
3. The tertiary loop allows controlling the temperature of the secondary cooling fluid by feeding cold water in a mixing vessel and extracting from it an equal flow of warm water.

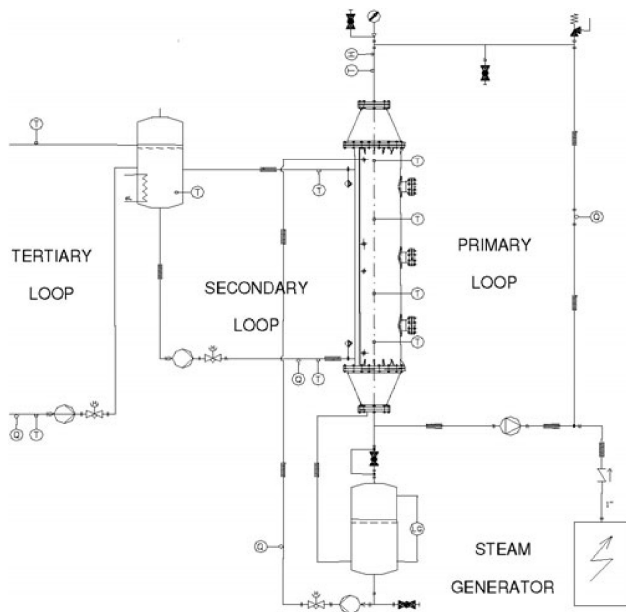


Fig. 2. Layout of the CONAN facility.

III.A. Main Features of the CONAN Facility

The primary loop contains the test section, consisting of an ~ 2 -m-long, 0.34-m side channel having square cross section, in which a mixture of steam, air, and helium is circulated. One of the lateral surfaces of the channel belongs to a 4.5-cm-thick aluminum flat plate, cooled on the back side by the water of the secondary loop. Condensation occurs on the inner surface of the cooled plate, and the related condensate flow is collected at its bottom by a gutter and routed by small-diameter piping to an external vessel; a relatively accurate estimate of the condensate flow is obtained by a differential pressure (i.e., level) measurement in this vessel. The other surfaces of the test section are kept reasonably insulated from the external environment to avoid condensation occurring over them.

Variable area sections connect the test section channel to the primary loop piping at both ends. The bottom part of the loop includes a variable speed blower for circulating the air-helium-steam mixture. Steam, produced by a 60-kW maximum power electrical steam generator, is injected at the bottom of the rising leg in the primary loop via a tee junction. The uppermost part of the primary loop is presently connected to the external atmosphere via an open pipe, to maintain atmospheric pressure conditions. The secondary loop includes a 5-mm-deep, 35-cm-wide rectangular cooling channel located on the back side of the aluminum plate, two collectors, and pipes for routing water at the outlet of the cooling channel to a mixing vessel, being a component common to the secondary and tertiary loops. The mixing vessel is

equipped with three heaters, with each one having a power of 3 kW, for warming up water during the startup phase and for controlling water temperature during operation. A pump located at the exit of the mixing vessel routes extracted water again to the secondary cooling channel. As mentioned above, the tertiary loop has the role of extracting cold water from a large reservoir available on the site, pumping it into the mixing vessel, and extracting an equal flow of warm water by free fall into an outlet pipe, thus obtaining the required power extraction from the secondary loop.

III.B. Operating Procedure

In the tests performed up to now, at atmospheric pressure, the main operating variables are

1. steam generator power, controlled by electronic equipment remotely operated in the facility control room
2. primary volumetric flow, adjusted to the prescribed values by varying the frequency of the electrical supply of the blower motor, through an inverter driven by related computer software
3. air-helium percentages, obtained by injecting helium into the primary circuit up to the desired concentration
4. secondary coolant temperature at the inlet of the cooling channel, controlled by changing the tertiary loop flow and the temperature set point of the heaters in the mixing vessel
5. secondary coolant flow rate.

For a fixed composition of the noncondensable gas mixture, once the steam generator power and the primary flow are fixed and the secondary coolant flow and temperature are set at the prescribed values, the primary mixture temperature and steam concentration are automatically defined. In fact, starting with a mixture rich in noncondensable gases, injecting steam through the steam generator outlet line and spontaneous purging of the excess noncondensable gases through the pipe open to the atmosphere increase steam concentration up to the point in which the obtained conditions allow an overall condensation rate equal to the inlet steam flow, provided this does not exceed the maximum system condensing capabilities. On the other hand, whenever the injected steam flow is lower than the condensation rate, the internal atmosphere tends to shrink, sucking noncondensable gases from the open pipe and decreasing the steam fraction down to a new equilibrium condition. Stable steady-state conditions are therefore achieved with steam very close to saturation conditions (appreciable superheating were never experienced), thus allowing investigation of a wide range of operating conditions. Tests are labeled as *Paa-Tbb-Vcc-Hee* or *aa-bb-cc-ee*, where

aa = nominal steam generator power (kW)

bb = nominal secondary coolant temperature at the inlet of the cooling channel (°C)

cc = nominal inlet velocity in tenths of m/s

dd = nominal molar fractions of helium in the non-condensable gas.

The main steps of the operating procedure are summarized:

1. The water stored in the secondary loop is heated up. This is performed by the three resistance heaters. During this heating-up phase, the pump of this loop also is running; the changes in the temperatures at the inlet and the outlet of the cooling section are measured, and the temporal changes are displayed on a personal computer screen.

2. The primary circuit blower and the steam generator are activated. This step aims at heating the primary circuit in order to minimize spurious condensation heat losses.

3. The primary flow rate is adjusted to achieve the desired inlet velocity in the test section.

4. The steam generator power is set to the desired operating value.

5. Helium is injected. The amount of helium is monitored to achieve the desired ratio to air, and it is continuously measured during the test.

6. The pump in the tertiary loop is activated and controlled, in order to evacuate from the secondary loop the heat released by condensation in the primary loop. The heaters in the mixing vessel compensate small unbalances.

Data coming from the measuring system are continuously acquired and monitored. Once steady-state conditions are reached, the available measures are recorded with a frequency of 0.5 Hz for periods of 600 s or more. The main measurements available in the facility are

1. temperature and relative humidity of the bulk mixture entering the test channel, estimated by temperature measurements through dry bulb and wet bulb thermal resistance
2. temperature of the bulk mixture at four locations along the centerline of the test section channel, by calibrated K-type thermocouples
3. level in the condensate collecting tank, by which the condensation rate is deduced
4. volumetric flow of the mixture in the primary circuit, measured by a vortex flowmeter
5. temperature at different locations and depths along and in the thickness of the aluminum plate,

by 1-mm K-type thermocouples inserted in 1.1-mm holes drilled in the plate

6. temperature of the secondary coolant in the inlet and outlet collectors
7. flow rate of the secondary coolant, via a Coriolis-type flowmeter
8. temperature of the tertiary coolant at the inlet and at the outlet of the mixing vessel
9. pressure in the primary vessel
10. helium molar fraction, obtained by conductivity measurements of the noncondensable air-helium mixture, after sampling the mixture at the inlet of the channel and condensing the steam.

III.C. Data-Processing Procedure

Several temperature measurements are available within the condensing plate, allowing one to obtain the local heat flux values at 18 different points. Given the temperature values TP_c and TP_h measured on the condensing plate for a particular axial location at a distance x from the inlet section, we obtain the corresponding transversal local heat flux Φ as

$$\Phi = -k \frac{dT}{dy} = -k \frac{\Delta T}{e_p} = k \frac{TP_c - TP_h}{e_p}, \quad (23)$$

where k is the thermal conductivity of the plate, estimated at the average temperature T_{avg} , defined as

$$T_{avg} = \frac{TP_c + TP_h}{2}. \quad (24)$$

The temperature on the surface of the condensing wall TP_i can also be estimated assuming a linear temperature profile across the aluminum plate:

$$TP_i = TP_c + (TP_h - TP_c) \frac{e'_p}{e_p}. \quad (25)$$

Once the heat fluxes are known, to know the local mass fluxes, we must separate the sensible heat transfer and the latent heat transfer contributions. If the assumption is retained that the condensate liquid film, whenever present, has negligible thickness and thus a negligible thermal resistance, the temperature at the condensing interface T_i can be assumed equal to the temperature estimated on the condensing wall TP_i . This conviction is confirmed by the experimental evidence that in the CONAN or in the CO-PAIN facilities³² (both square cross-section channels, 2 m long), a continuous liquid film is highly unlikely even for the largest condensation rates. On the contrary, the condensate tends to form droplets or liquid rivulets wetting only a small portion of the condensing plate, as shown in Fig. 3 for a high condensation mass flux and high free

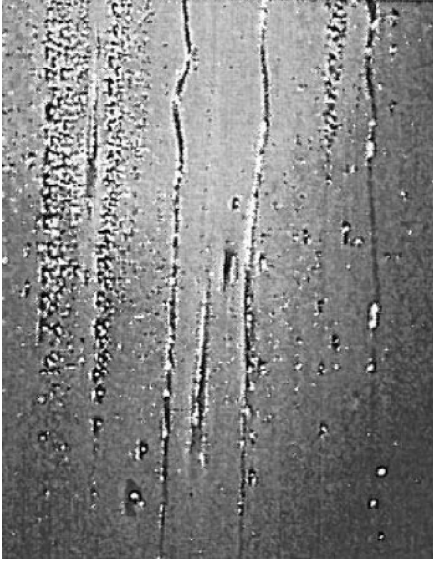


Fig. 3. View of the COPAIN condensing plate during a test at high mass transfer and high free stream velocity.

stream velocity in the COPAIN facility.³² As a consequence, it is

$$\Phi = \underbrace{\Phi_s}_{\text{sensible}} + \underbrace{\dot{m}''_{v,i} h_{lv,i}}_{\text{latent}}, \quad (26)$$

where Φ_s and $\dot{m}''_{v,i} h_{lv,i}$ are the local sensible heat flux and the local latent heat flux, respectively. Moreover, the ratio between the sensible heat flux and the condensation mass flux can be written as follows:

$$\frac{\Phi_s}{\dot{m}''_{v,i}} = \frac{h_s \Delta T}{h_m B_m} = \frac{\text{Nu}_x K/x (TP_i - T_b)}{\text{Sh}_x \rho D_{vm}/x \left(\frac{Y_{v,i} - Y_{v,b}}{1 - Y_{v,i}} \right)}, \quad (27)$$

where

$Y_{v,i}$ = local steam mass fraction at the interface

$Y_{v,b}$ = steam mass fraction in the bulk.

Here, the analogy between heat and mass transfer is introduced:

$$\frac{\text{Nu}_{0,x}}{\text{Sh}_{0,x}} = \left(\frac{\text{Pr}}{\text{Sc}} \right)^{1/3}. \quad (28)$$

To extend the validity of the heat and mass transfer analogy to high condensation rates, we introduce the Stefan factor F (Ref. 29) and the Ackerman factor A (Ref. 33), defined as

$$F = \frac{\Phi_m}{e^{\Phi_m} - 1} \quad \text{and} \quad A = \frac{\Phi_t}{e^{\Phi_t} - 1} \quad (29)$$

with

$$\Phi_m = \frac{\dot{m}''_{v,i}}{h_{m,0}} \quad \text{and} \quad \Phi_t = \frac{\dot{m}''_{v,i} C_{p,v,i}}{h_{s,0}}. \quad (30)$$

Since it is reasonable to assume that $F \sim A$, the heat and mass transfer analogy can be turned to obtain

$$\left(\frac{\text{Pr}}{\text{Sc}} \right)^{1/3} = \frac{\text{Nu}_{0,x}}{\text{Sh}_{0,x}} = \frac{\text{Nu}_x}{A} \frac{F}{\text{Sh}_x} \sim \frac{\text{Nu}_x}{\text{Sh}_x}. \quad (31)$$

After some mathematical manipulations, the ratio between average sensible heat flux and mass flux is given by

$$\frac{\Phi_s}{\dot{m}''_{v,i}} = \frac{C_p (TP_i - T_b)}{\left(\frac{Y_{v,i} - Y_{v,b}}{1 - Y_{v,i}} \right)} \left(\frac{\text{Sc}}{\text{Pr}} \right)^{2/3} = \frac{C_p (TP_i - T_b)}{\left(\frac{Y_{v,i} - Y_{v,b}}{1 - Y_{v,i}} \right)} \text{Le}^{2/3}. \quad (32)$$

The local sensible heat flux Φ_s and the local condensation mass flux $\dot{m}''_{v,i}$ are therefore obtained by solving simultaneously Eqs. (26) and (32). The experimental local Sherwood number Sh_x can be finally calculated by

$$\text{Sh}_x = \frac{\dot{m}''_{v,i} x}{\rho D_{vm} B_m} = \frac{\dot{m}''_{v,i} x}{\rho D_{vm}} \left(\frac{1 - Y_{v,i}}{Y_{v,i} - Y_{v,b}} \right). \quad (33)$$

The corrected local Sherwood number, deprived of suction effects, is instead given by

$$\text{Sh}_{0,x} = \frac{\dot{m}''_{v,i} x}{\rho D_{vm} F B_m} = \frac{\dot{m}''_{v,i} x}{\rho D_{vm}} \left(\ln \frac{Y_{nc,b}}{Y_{nc,i}} \right)^{-1}. \quad (34)$$

Similarly, the local Nusselt number is given by

$$\text{Nu}_x = \frac{\Phi_s x}{k (TP_i - T_b)}. \quad (35)$$

All properties appearing in the definition of the Sherwood or the Nusselt numbers are defined as film properties, and their value is calculated according to the following rules:

$$\rho = \frac{\rho_i + \rho_b}{2} \quad \text{and} \quad D_{vm} = \frac{D_{vm,i} + D_{vm,b}}{2};$$

$$k = \frac{k_i + k_b}{2} \quad \text{and} \quad C_p = \frac{C_{p,i} + C_{p,b}}{2}. \quad (36)$$

All these quantities are functions of the temperature at the condensing interface and of the bulk temperature,

as well as the mixture composition defined by the species molar fraction. For this reason the helium-to-noncondensable gas ratio

$$\chi = \frac{X_{he}}{X_a + X_{he}} \quad (37)$$

must be known both in the bulk and at the condensing interface. Since the value is measured only in bulk, the interface value must be evaluated. It can be assumed that because of convection and turbulence effects, in turbulent condensing boundary layers it is²⁷

$$\chi_i = \chi_b \quad (38)$$

This assumption translates the conviction that owing to the overwhelming effects of turbulence in the boundary layer, the different molecular mobility of mixture components has a little role in the near-wall region.

III.D. Uncertainty on Experimental Heat Fluxes

Temperature measurements TP_c and TP_h contribute to the reduction of local heat fluxes and introduce measurement uncertainties. The typical standard deviation obtained for temperature measurements is of the order of 0.25 K. The nominal distance between the two thermocouples is 17 mm, but a standard deviation of 0.5 mm was assumed to include manufacturing imperfections. Last but not least, the uncertainty on the thermal conductivity of the condensing plate was accounted for, considering a standard deviation of 5%. This accounts for uncertainties on the formula correlating the thermal conductivity of the material with temperature, and uncertainties around the nominal value of the average temperature T_{avg} . The uncertainty on local heat fluxes was therefore deduced based on the error propagation theory.³⁴ It was ascertained that standard deviations σ on local heat fluxes do not exceed 7% of the average values for all tests (in Figs. 20 through 23, heat fluxes are reported with error bands $\pm 2\sigma$).

IV. ANALYSIS OF EXPERIMENTAL DATA

Two main physical properties differentiate a noncondensable light gas and air: molecular diffusivity and molecular weight. To investigate the effect of helium on steam condensation, we have thus divided the analysis into two parts: forced convection condensation, focusing on the effect of diffusivity, and natural convection condensation, combining both diffusivity and buoyancy effects. Two different experimental campaigns and two series of computations have been carried out with a multiple purpose: to qualify experimental data, to validate CFD models, and to achieve information on the involved phenomena.

IV.A. Forced Convection Tests

Eighteen forced convection tests have been performed in this campaign. Two different nominal power levels of the steam generator (20 and 25 kW), five different mixture velocities (1.5, 2.0, 2.5, 3.0, and 3.5 m/s), and different helium concentrations (from 0 to 75% of the total amount of noncondensable gases) were considered.

A useful way for analyzing experimental results consists of comparing local experimental Sherwood numbers deduced by measurements, as shown in Eq. (34), to those predicted by the analogy between heat and mass transfer, adopting an appropriate correlation, which in turbulent forced convection could be Eq. (20).

In Figs. 4 and 5, the results of this analysis are shown for the series at 20 and 25 kW, respectively, together with the composition of the inlet mixture. Remarkable

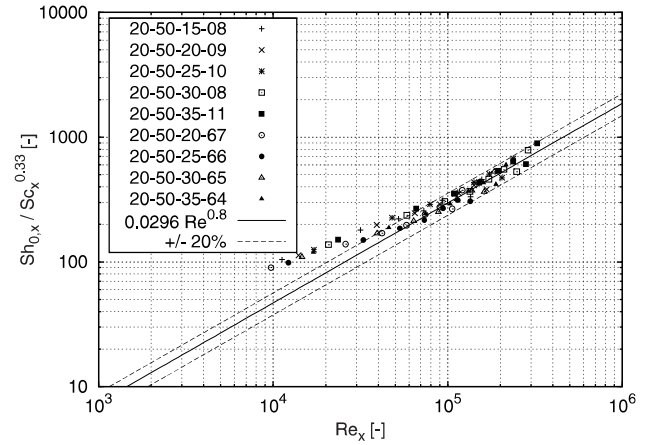


Fig. 4. Experimental Sherwood number $Sh_{0,x}$ in forced convection tests at 20 kW.

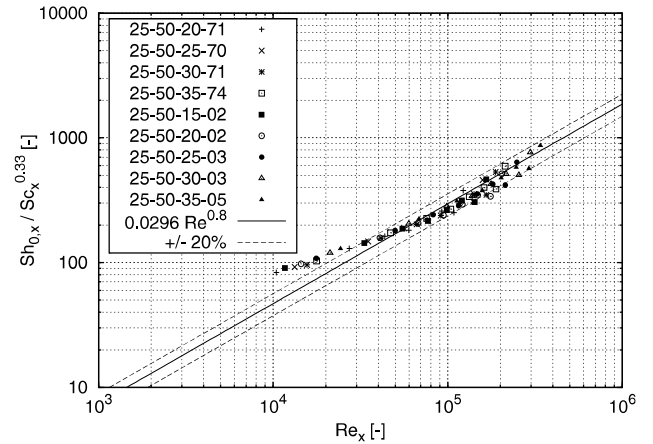


Fig. 5. Experimental Sherwood number $Sh_{0,x}$ in forced convection tests at 25 kW.

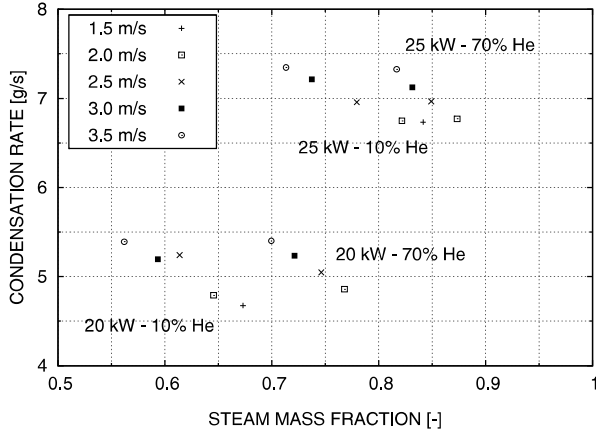


Fig. 6. Overall condensation rates versus steam mass fraction in forced convection tests.

agreement of experimental Sherwood number points with the Schlichting correlation is observed for Reynolds numbers $>10^5$. As a conclusion, for fully developed forced convection condensation, the heat and mass transfer analogy is capable of providing an appropriate description of phenomena.

As said in Sec. III.B, in the CONAN facility, for a given helium percentage, once the steam generator and the primary flow are fixed and the secondary coolant flow and temperature are set to the prescribed values, the primary temperature and steam concentration are automatically defined, and so is the condensation rate. This is confirmed by experimental results shown in Fig. 6. On one hand, helium improves the diffusivity of steam and makes the steam mass fraction increase (see Figs. 7 and 8), resulting in an increase of the driving force that is approximately given by $\ln(1 - Y_{v,b})$. On the other hand,

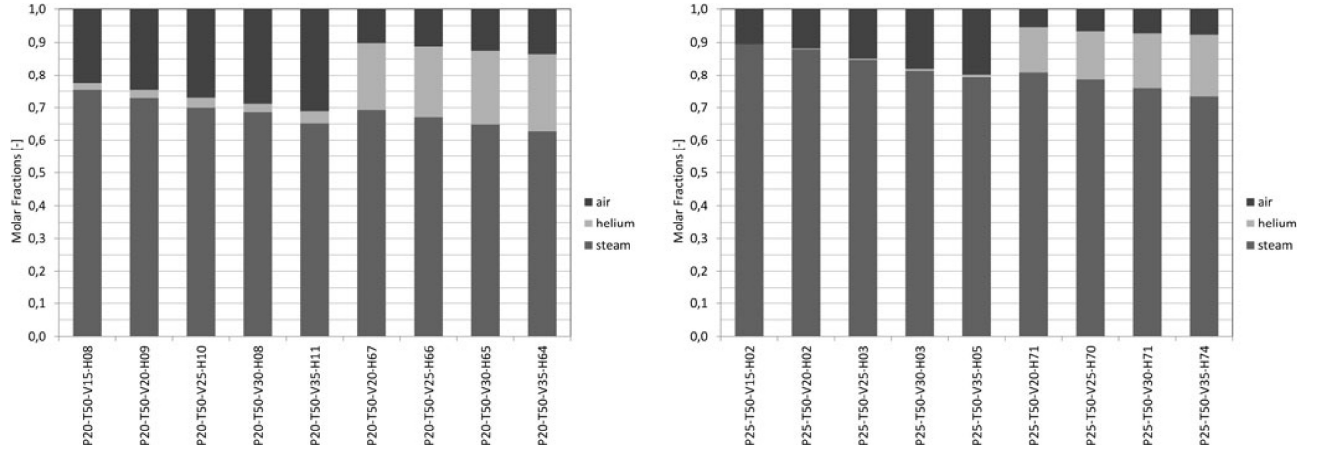


Fig. 7. Mixture composition (molar fractions) in forced convection tests at 20 kW and 25 kW.

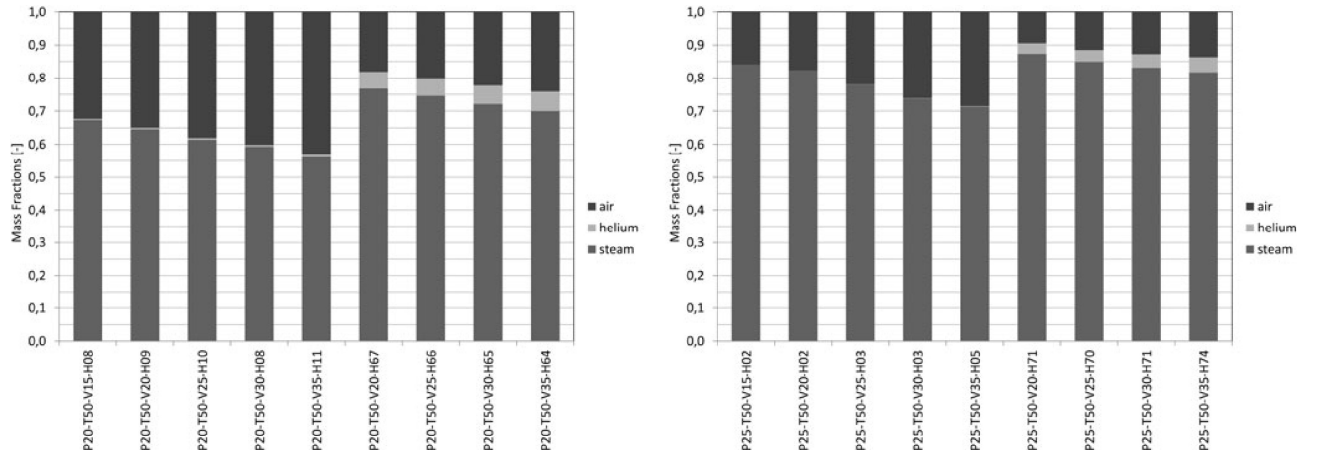


Fig. 8. Mixture composition (mass fractions) in forced convection tests at 20 kW and 25 kW.

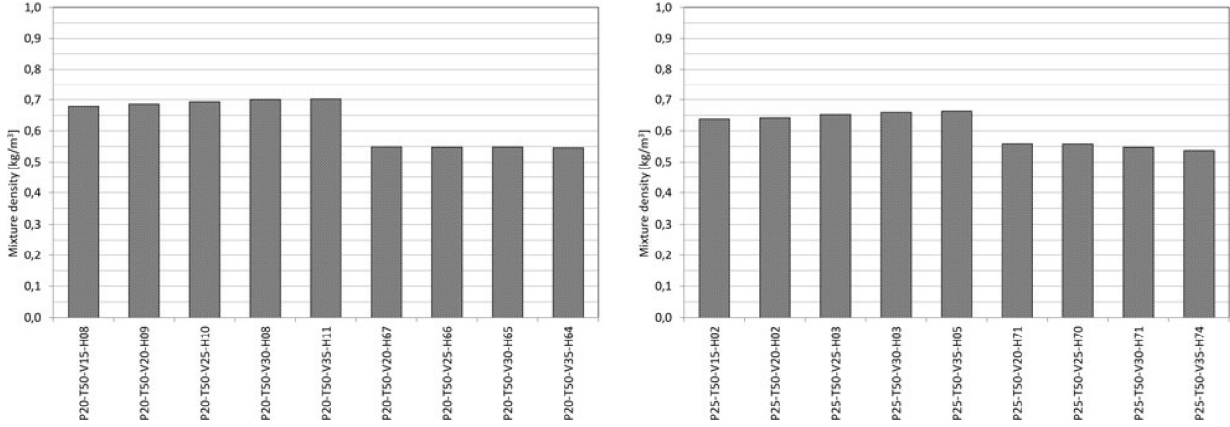


Fig. 9. Mixture density in forced convection tests at 20 kW and 25 kW.

the mixture density is reduced (see Fig. 9), resulting in a decrease of the maximum attainable Reynolds and Sherwood numbers.

However, it can be shown that for a given Reynolds number (and therefore a given Sherwood number), increasing helium concentration seems to have a positive effect on the condensation rate (see the trends of experimental condensation rates for the two series at 20 and 25 kW in Fig. 10): In this case the increase of molecular diffusivity results in an increase of the mass transfer coefficient and of the condensation rate.

Other formulations of the heat and mass transfer analogy have been used to analyze experimental data. It is known that the various forms of the heat and mass transfer analogy can be roughly divided into two main categories: those cast in terms of mass fractions and therefore adopting a mass approach and those cast in terms of molar fractions, thus adopting a molar approach. In the present work, results available by the CONAN facility

have been presented according to a formulation cast in terms of mass fractions, as reported in Spalding³⁵ or Lienhard.³⁶ However, in past studies, Ambrosini et al.³⁷ investigated the different forms of the heat and mass transfer analogy and quantified differences among the different formulations in the analysis of CONAN steam-air condensation tests. In particular, they investigated the difference between the mass approach and the molar formulations of Chilton and Colburn³⁸ and Peterson et al.³⁹; they showed that formulations based on the molar approach give higher Sherwood numbers with respect to the formulation based on the mass approach, but the differences were relatively small ($< 10\%$) in relevant parameter ranges. In this section, the mass approach formulation is compared to the formulation of Bird et al.⁴⁰ and Peterson et al.,³⁹ for which the local Sherwood numbers are given, respectively, by

$$Sh_{0,x,molar} = \frac{\dot{m}''_{v,i} x}{M_v c D_{vm}} \left(\ln \frac{X_{nc,b}}{X_{nc,i}} \right)^{-1} \quad (39)$$

and

$$Sh_{0,x,Peterson} = \dot{m}''_{v,i} x \frac{h_{lv}}{k_c (T_i - T_{sat}(P_{v,b}))} \quad (40)$$

with

$$k_c = \frac{M_v^2 h_{lv}^2 P_0 D_{vm}^0}{\Phi T_{avg} R^2 T_0^2},$$

$$\Phi = - \frac{\ln \frac{1 - X_{nc,b}}{1 - X_{nc,i}}}{\ln \frac{X_{nc,b}}{X_{nc,i}}},$$

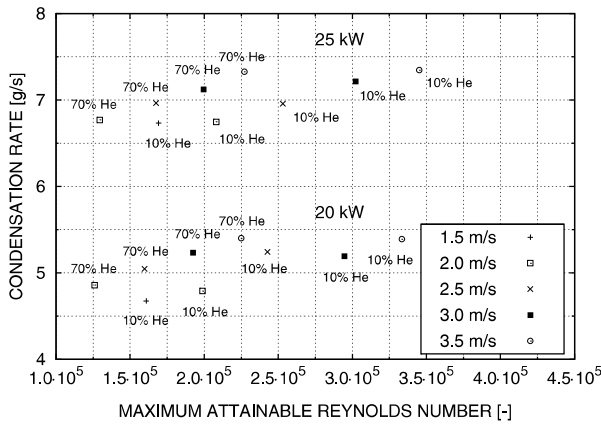


Fig. 10. Overall condensation rates versus maximum attainable Reynolds numbers in forced convection tests.

and

$$T_{avg} = \frac{T_i + T_{sat}(P_{v,b})}{2} \quad (41)$$

For a given experimental mass flux $\dot{m}''_{v,i}$, the ratio between the Sherwood number predicted by the molar approach by Eq. (39) and the mass approach by Eq. (34) is given by

$$\frac{Sh_{0,x,molar}}{Sh_{0,x}} = \frac{M}{M_v} \frac{\ln \frac{M_i X_{nc,b}}{M_b X_{nc,i}}}{\ln \frac{X_{nc,b}}{X_{nc,i}}}, \quad (42)$$

where it was assumed that $\chi_i = \chi_b = \chi$, $M = \rho/c$, and $M_b = X_{v,b}M_v + (1 - X_{v,b})(\chi M_{he} + (1 - \chi)M_a)$

and

$$M_i = X_{v,i}M_v + (1 - X_{v,i})(\chi M_{he} + (1 - \chi)M_a) \quad (43)$$

Differently from the case of binary mixtures of steam and air, for which the ratio expressed by Eq. (42) is always >1 , in steam-air-helium mixtures this ratio can be lower than unity. Indeed, depending on the helium concentration, the mixture molecular weight at the interface can be even lower than in bulk. Figure 11 compares the mass and the molar formulations, together with the theoretical predictions obtained by Eq. (42) considering the average bulk and interface temperatures of the selected experimental series. As can be deduced from Fig. 11, when the interface mixture is heavier than the bulk mixture, the molar approach tends to give higher Sherwood number values. On the contrary, if the interface mixture is lighter than the bulk, which occurs for high helium concentra-

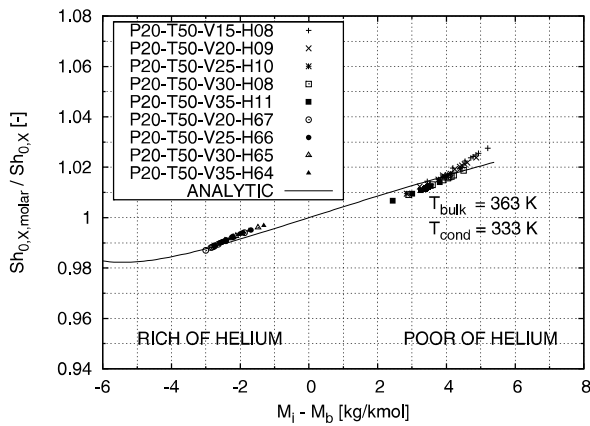


Fig. 11. Ratio of the Sherwood numbers calculated according to Bird and Lienhard models.

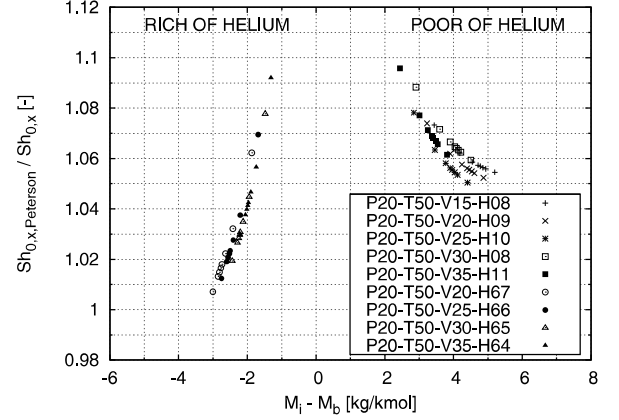


Fig. 12. Ratio of the Sherwood numbers calculated according to Peterson and Lienhard models.

tions in bulk, the molar approach predicts lower values. The Peterson model is also compared to the mass formulation in Fig. 12. Differently from the molar approach, for the addressed experimental data, the ratio between the Sherwood numbers in Eqs. (40) and (34) is generally higher than unity. Moreover, very large differences could be experienced when the interface and bulk mixtures have similar molecular weights.

IV.B. Buoyancy Effects in Low-Velocity Tests

A second experimental campaign was performed to investigate buoyancy effects induced by helium (e.g., of the order of 0.6 m/s). Low-velocity tests were thus performed with different helium concentrations. In condensing mixtures of steam and air, the fluid close to the interface is heavier than in bulk, since the condensing interface is cold and rich of air. Natural convection regimes are established if buoyancy forces are strong enough to overwhelm inertia forces. In the presence of large quantities of helium, however, the difference in weight between the interface and bulk density can be reduced. For certain helium concentrations the density difference can even be annealed, and forced convection regimes can thus be experienced even at low velocities since buoyancy becomes irrelevant. This phenomenon has been observed in CONAN tests with helium concentrations in bulk close to $\sim 62\%$ (see Figs. 13 and 14). While for low concentrations of helium a natural convection regime is experienced [see Fig. 15, blue dashed line (color online only)], for tests at high helium concentration (around 60%), the comparison between experimental asymptotic Sherwood numbers and correlations for forced and natural convection (Schlichting and McAdams, respectively) pointed out the presence of a forced convection regime (black dashed line).

The transition between the steam-air natural convection regime and the steam-air-helium mixture convection

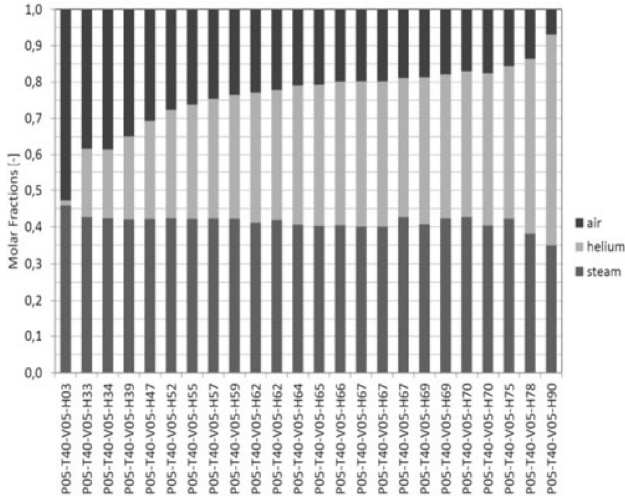


Fig. 13. Mixture composition in condensation tests at low velocity.

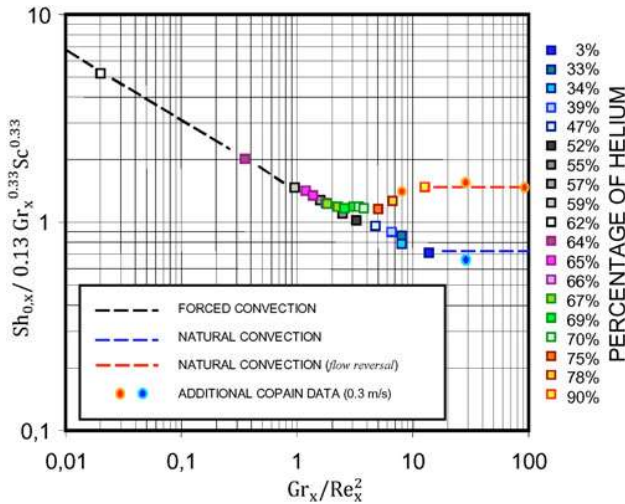


Fig. 14. Richardson number in condensation tests at low velocity.

regime is investigated in Fig. 16. Experiments and computations confirm a progressive reduction of the Sherwood number from 0% to 60% of helium, due to a reduction of buoyancy forces. However, the most interesting phenomena have been observed with helium concentrations $>62\%$. For these concentrations an inverse density gradient establishes, since the density at the interface is lower than the bulk density. This phenomenon is here referred to as *buoyancy reversal*: Buoyancy and inertia forces act in opposite directions. If reversed buoyancy forces are strong enough, a local inversion of

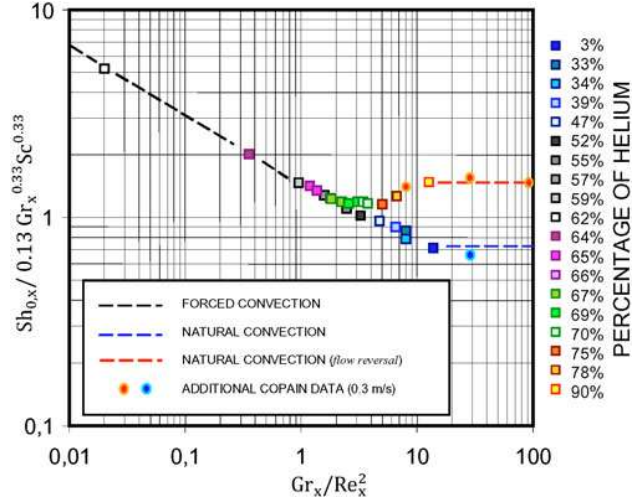


Fig. 15. Experimental Sherwood number in condensation tests at low velocity.

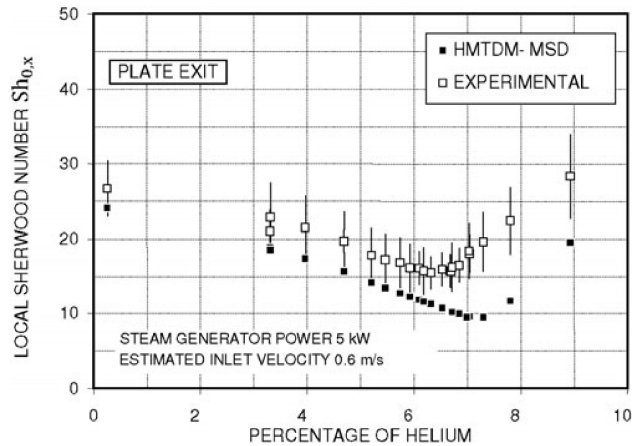


Fig. 16. Buoyancy reversal in CONAN tests at low velocity.

the velocity field can even be experienced. This phenomenon, named *flow reversal*, is clearly reproduced by HMTDMs, e.g., for tests at 90% of helium (see Fig. 17), but experimental data suggest its presence also for tests at lower concentrations (see Fig. 16). Indeed, the phenomenon is associated with a sharp increase of the mass transfer coefficient and the condensation rate. As shown in Fig. 15, a natural convection regime is established with improved mass transfer characteristics (red dashed line). Detailed computations show that the occurrence of buoyancy reversal and the subsequent flow reversal involves a significant increase in turbulence in the near-wall region, which is suggested as one of the causes of improved mass transfer with respect to steam-air natural convection.

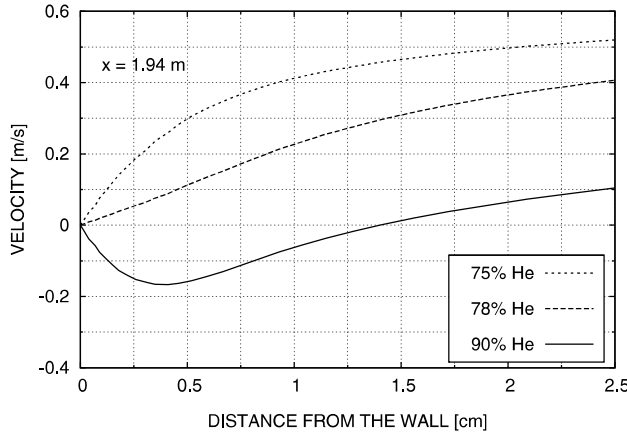


Fig. 17. Predicted flow reversal in CONAN tests at low velocity near the plate exit.

V. RESULTS OF COMPUTATIONS

Computations have been performed with the FLU-ENT code, where three different condensation models have been implemented. Turbulence effects have been modeled with the $\kappa - \varepsilon$ model. To deal with near-wall turbulence, we used the FLUENT EWT with the HMTDMs (EBD and MSD), whereas standard logarithmic wall functions have been used with HMTAM. An overview on the performance of the condensation models is given in Figs. 18 and 19, where the overall condensation rates calculated by the three models are compared to the experimental rates. The overall behavior of the models is satisfactory for both the forced convection and the low-velocity cases. A relatively poorer prediction of local heat and mass transfer rates has been ascertained in the entrance region (see Figs. 20 through

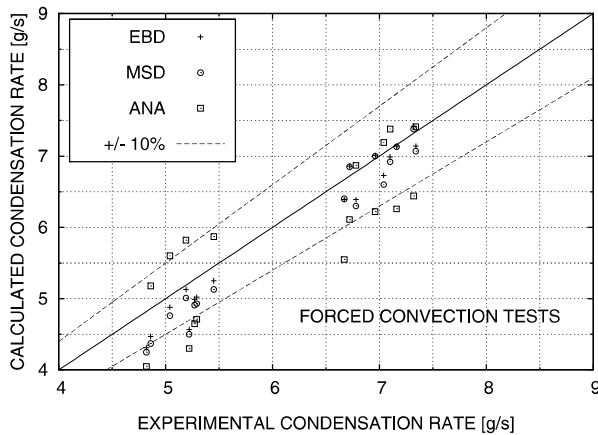


Fig. 18. Comparison between calculated and experimental condensation rates in forced convection conditions.

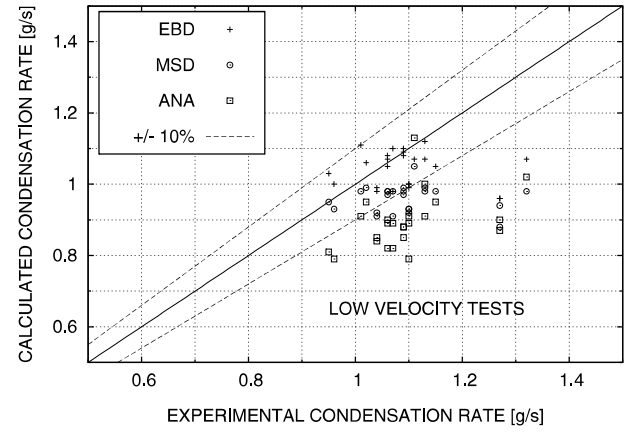


Fig. 19. Comparison between calculated and experimental condensation rates in low-velocity tests.

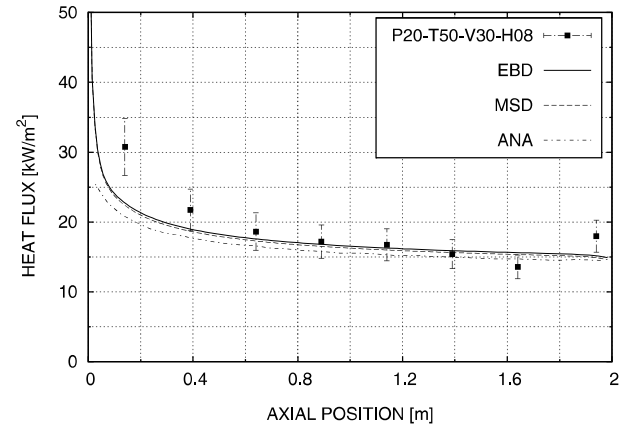


Fig. 20. Comparison between calculated and experimental heat fluxes (forced convection-low helium concentration).

23), which could have caused a slight underestimation of overall condensation rates. Indeed, even if the asymptotic behavior of local heat fluxes is correctly reproduced, a lack of accuracy affects the description of the developing region next to the inlet section, for which the selected turbulence models are less appropriate. The actual distribution of flow velocity at the test section inlet is also hardly expected to be completely flat as assumed in calculations, introducing other justifications for the observed discrepancy. Important information deduced by analyzing local heat fluxes is also that, in turbulent forced convection condensation, only minor differences must be expected between EBD and MSD: As expected, the more important turbulent diffusion is, the more similar are the results obtained by the two formulations. Finally, the trend of local heat flux predicted by EBD and MSD for the case at low velocity and high helium concentration (see Fig. 23) is worth

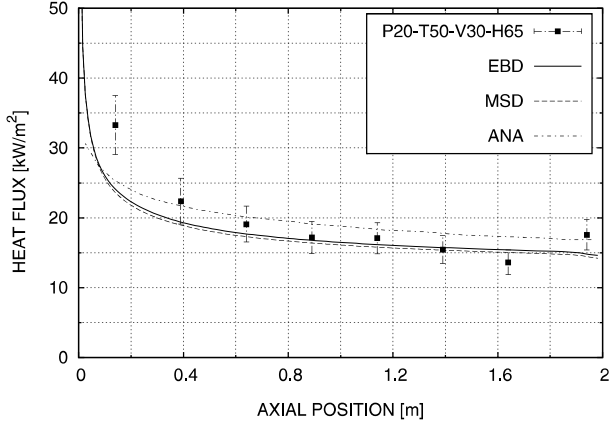


Fig. 21. Comparison between calculated and experimental heat fluxes (forced convection–high helium concentration).

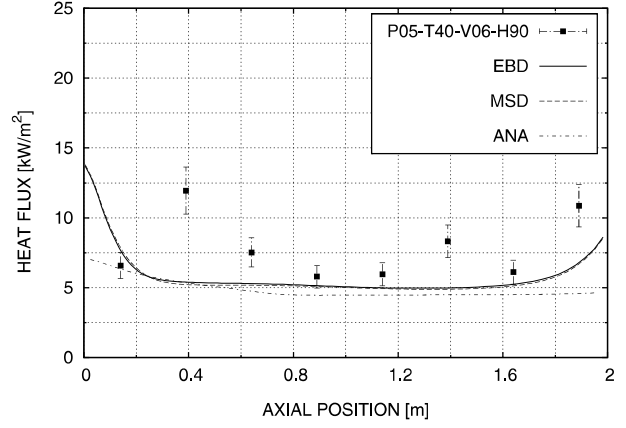


Fig. 23. Comparison between calculated and experimental heat fluxes (low velocity–high helium concentration).

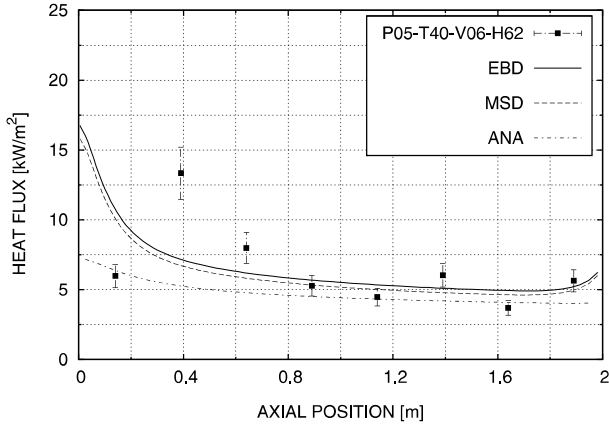


Fig. 22. Comparison between calculated and experimental heat fluxes (low velocity–low helium concentration).

considering. Near the outlet section of the channel, a sharp increase of the experimental heat flux is ascertained, reproduced correctly by the HMTDMs. This phenomenon is attributed to the presence of flow reversal, as shown in Fig. 17.

VI. SCALING OF CONDENSATION TESTS FOR HYDROGEN SAFETY ANALYSIS

Based on the molar formulation of the heat and mass transfer analogy, we can find simple scaling criteria, estimating the ratio of the local condensation rates for mixtures of steam-air-hydrogen (labeled with h_2) and steam-air-helium (labeled with he) having equivalent molar concentration. As in the previous analyses, the

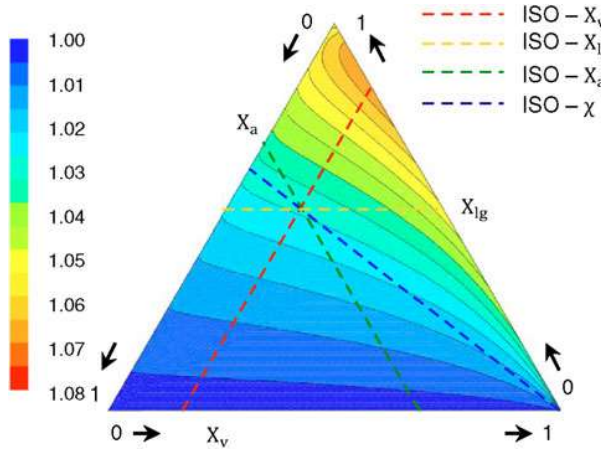
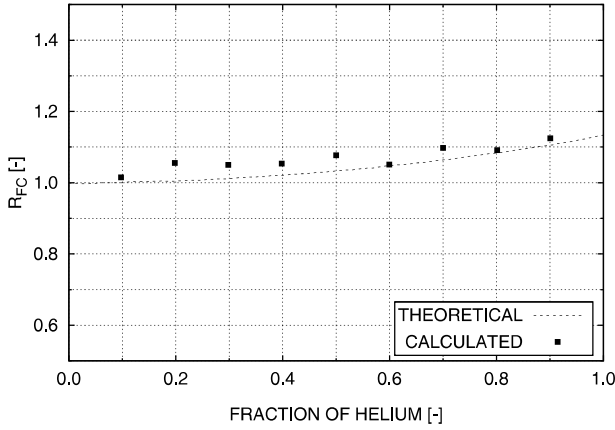
cases of forced convection and low velocity have to be treated separately.

VI.A. Scaling of Forced Convection Tests

Based on the Schlichting correlation, we can express in forced convection conditions, for a given mixture inlet velocity and temperature boundary conditions, the ratio

$$R_{FC} = \frac{\dot{m}''_{v,i}(h_2)}{\dot{m}''_{v,i}(he)} = \left(\frac{D_{vm}(h_2)}{D_{vm}(he)} \right)^{2/3} \left(\frac{\mu(h_2)}{\mu(he)} \right)^{-7/15} \times \left(\frac{\rho(h_2)}{\rho(he)} \right)^{7/15}. \quad (44)$$

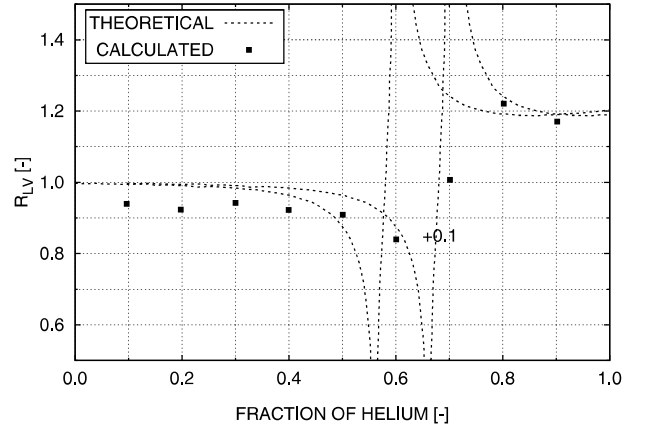
A scaling criterion can thus be established simply based on film properties, which are the properties of the mixture evaluated at the average temperature between the bulk and the condensing interface. The quantity R_{FC} can be plotted in triangular diagrams where the three axes represent the molar fractions of the three species (see Fig. 24). Moreover, since steam is considered in saturation conditions, as in actual CONAN tests, if the mixture is assumed to behave as an ideal gas mixture, the steam molar fraction can be occasionally replaced by the steam saturation temperature corresponding to its partial pressure. As a consequence, the lines representing constant steam molar fraction are also at constant temperature. The theoretical correlation proposed above has been tested against the prediction of the MSD model, proving the consistency of the analysis. For the sake of simplicity, a single case having 30°C of condensation temperature and 90°C of bulk (inlet) temperature is considered. The line identifying the intersection of R_{FC} with the steam molar fraction corresponding to a film temperature (60°C) is reported in Fig. 25 (dashed line). In Fig. 25, the values

Fig. 24. R_{FC} at atmospheric pressure.Fig. 25. Comparison between theoretical and calculated R_{FC} at atmospheric pressure and 60°C of film temperature.

predicted by CFD computations performed with the MSD model are reported. The results of this analysis allow us to conclude that mixtures of hydrogen and helium having the same molar concentrations give similar mass fluxes in forced convection.

VI.B. Scaling of Low-Velocity Tests

Contrary to forced convection, in the presence of buoyancy forces, the ratio of the local condensation rates for mixtures of steam-air-hydrogen and steam-air-helium cannot be expressed as a simple function of film properties. This is because in buoyancy-driven flow, the velocity scale is not assigned independently but is intrinsically defined by the density difference between the condensing wall and the bulk. Based on the McAdams correlation, we obtain the following relationship:

Fig. 26. Comparison between theoretical and calculated R_{LV} at atmospheric pressure, 30°C of condensation surface temperature and 90°C of bulk temperature.

$$R_{LV} = \frac{\dot{m}''_{v,i}(h_2)}{\dot{m}''_{v,i}(he)} = \left(\frac{D_{vm}(h_2)}{D_{vm}(he)} \right)^{2/3} \left(\frac{\mu(h_2)}{\mu(he)} \right)^{-1/3} \times \left(\frac{\Delta\rho(h_2)}{\Delta\rho(he)} \right)^{1/3}, \quad (45)$$

consisting of a film properties function, given by the product of density and viscosity ratios, and a function of density differences. Considering the same temperature conditions as the forced convection case, we compare the term and computational results in Fig. 26. The same phenomena described for helium tests must be expected, but buoyancy and flow reversal would occur in hydrogen tests for lower molar concentrations of the light gas, since hydrogen is lighter than helium.

VII. CONCLUSIONS

Condensation phenomena in the presence of light noncondensable gases have been investigated in this work. The synergy between experimental and computational analyses has allowed consolidating knowledge about forced and natural convection condensation, focusing on peculiar phenomena occurring in the presence of buoyancy effects. Indeed, a better understanding of buoyancy and flow reversal effects has been achieved, made possible by simultaneous experimental and computational investigations.

We have developed and validated different CFD models, adopting different modeling strategies and having different purposes. All models are capable of correctly reproducing the phenomena involved in steam-air-helium condensation tests, confirming also the reliability of experimental results. An experimental database is therefore

made available for the validation of codes. Finally, simple criteria for scaling of condensation tests in the presence of a light gas have been provided, demonstrating the suitability of helium as a substitute for hydrogen and thus reinforcing the confidence in present and previous studies making use of this substitution and providing relevant guidelines for the design of future experimental investigations.

NOMENCLATURE

A	= matrix of MSD
<i>A</i>	= Ackerman suction factor
<i>B_m</i>	= condensation driving force
<i>D</i>	= diffusion coefficient (m ² /s)
<i>e</i>	= internal energy (J/kg)
<i>F</i>	= Stefan suction factor
g	= gravity (m/s ²)
<i>h</i>	= enthalpy (J/kg)
<i>h_m</i>	= mass transfer coefficient (kg/m ² ·s ⁻¹)
j	= diffusion mass flux vector (kg/m ² ·s ⁻¹)
<i>k</i>	= thermal conductivity (W/m·K ⁻¹)
<i>M</i>	= molecular weight (kg/kmol)
<i>m''_{v,i}</i>	= condensation mass flux (kg/m ² ·s ⁻¹)
n_i	= outer oriented normal
<i>P</i>	= pressure (Pa)
<i>R</i>	= scaling factor
S	= vectorial source term (units/m ³)
<i>S</i>	= scalar source term (units/m ³)
<i>T, TP</i>	= temperature (K)
<i>t</i>	= time (s)
u	= velocity vector (m/s)
<i>u</i>	= velocity module (m/s)
<i>X</i>	= molar fraction
<i>x</i>	= spatial coordinate (m)
<i>Y</i>	= mass fraction

Greek

α	= thermal diffusivity (m ² /s)
ε	= turbulent kinetic energy dissipation (m ² /s ³)
κ	= turbulent kinetic energy (m ² /s ²)
μ	= dynamic viscosity (kg/m·s ⁻¹)

ν	= kinematic viscosity (m ² /s)
ρ	= density (kg/m ³)
τ	= shear stress tensor (Pa)
χ	= helium-to-noncondensable-gas ratio

Subscripts

<i>a</i>	= air
<i>c</i>	= near-wall cell, or cold
<i>FC</i>	= forced convection
<i>h</i>	= enthalpy, or hot
<i>i</i>	= condensing interface
<i>j</i>	= species <i>j</i>
<i>k</i>	= species <i>k</i>
<i>LV</i>	= low velocity
<i>l</i>	= liquid
<i>lg</i>	= light gas
<i>MC</i>	= mixed convection
<i>m</i>	= mass or mixture
<i>NC</i>	= natural convection
<i>nc</i>	= noncondensables
<i>p</i>	= condensing plate
<i>q</i>	= momentum
<i>t</i>	= turbulence
<i>v</i>	= vapor

Dimensionless Numbers

Gr_x	= local Grashof number = $\rho g \Delta \rho x^3 / \mu^2$
Le	= Lewis number = α / D_{vm}
Pr	= Prandtl number = ν / α
Re_x	= local Reynolds number = $\rho u x / \mu$
Sc	= Schmidt number = ν / D_{vm}
Sh_x	= local Sherwood number = $h_m x / \rho / D_{vm}$
$Sh_{0,x}$	= local Sherwood number = $h_{m,0} x / \rho / D_{vm}$

REFERENCES

1. M. L. CORRADINI, "Turbulent Condensation on a Cold Wall in the Presence of a Noncondensable Gas," *Heat Transfer Fluid Flow*, **64**, 186 (Feb. 1984).

2. A. A. DEHBI, "The Effects of Noncondensable Gases on Steam Condensation Under Turbulent Natural Convection Conditions," PhD Thesis, Massachusetts Institute of Technology (Jan. 1991).
3. I. K. HUHTINIEMI, "Condensation in the Presence of a Noncondensable Gas: The Effect of Surface Orientation," PhD Thesis, University of Wisconsin (1991).
4. K. M. VIEROW and V. E. SCHROCK, "An Experimental Investigation of the Effect of Air on Steam Condensation Under Turbulent Natural Convection, Part 1—Heat Transfer," *Proc. Int. Conf. Multiphase Flow*, Tsukuba, Japan, September 1991.
5. D. G. OGG, "Vertical Downflow Condensation Heat Transfer in Gas-Steam Mixtures," Master's Thesis, Department of Nuclear Engineering, University of California, Berkeley (Jan. 1991).
6. M. SIDDIQUE, "The Effects of Noncondensable Gases on Steam Condensation Under Forced Convection Conditions," PhD Thesis, Department of Nuclear Engineering, Massachusetts Institute of Technology (Jan. 1991).
7. M. SIDDIQUE, M. W. GOLAY, and M. S. KAZIMI, "Local Heat Transfer Coefficients for Forced-Convection Condensation of Steam in a Vertical Tube in the Presence of a Noncondensable Gas," *Nucl. Technol.*, **102**, 386 (1993).
8. I. K. HUHTINIEMI and M. L. CORRADINI, "Condensation in the Presence of Noncondensable Gases," *Nucl. Eng. Des.*, **141**, 429 (1993).
9. S. Z. KUHN, V. E. SCHROCK, and P. F. PETERSON, "An Investigation of Condensation from Steam-Gas Mixtures Flowing Downward Inside a Vertical Tube," *Nucl. Eng. Des.*, **177**, 53 (1997).
10. M. H. ANDERSON, L. E. HERRANZ, and M. L. CORRADINI, "Experimental Analysis of Heat Transfer Within the AP600 Containment Under Postulated Accident Conditions," *Nucl. Eng. Des.*, **185**, 153 (1998).
11. K. FISCHER et al., "Containment Code Comparison Exercise on Experiment ThAI TH7," *Proc. 10th Int. Topl. Mtg. Nuclear Reactor Thermal Hydraulics (NURETH-10)*, Seoul, Korea, October 5–9, 2003.
12. L. BLUMENFELD and H. PAILLERE, "CFD Simulation of Mixed Convection and Condensation in a Reactor Containment: The MICOCO Benchmark," *Proc. 10th Int. Topl. Mtg. Nuclear Reactor Thermal Hydraulics (NURETH-10)*, Seoul, Korea, October 5–9, 2003.
13. H. J. ALLELEIN et al., "International Standard Problem ISP-47 on Containment Thermal-Hydraulics," Technical Report 10, Organisation for Economic Co-operation and Development/Nuclear Energy Agency/Committee on the Safety of Nuclear Installations (2007).
14. W. AMBROSINI et al., "CFD Models for Predicting Condensation in Nuclear Reactor Containments Within the SARnet Network of Excellence," SARNET-CONT-P02, SARnet (2006).
15. W. AMBROSINI et al., "Comparison and Analysis of the Condensation Benchmark Results," *Proc. 3rd European Mtg. Severe Accident Research (ERMSAR-2008)*, Nessebar, Bulgaria, September 23–25, 2008.
16. D. LIOCE, "Prove sperimentali di condensazione di miscele ternarie di aria, elio-vapore e qualifica mediante un codice di CFD," Master's Thesis, University of Pisa (2006).
17. F. POLI, "Prove sperimentali sulla condensazione a film di miscele ternarie aria-elio-vapore e qualifica dei dati mediante un codice di CFD," Master's Thesis, University of Pisa (2007).
18. M. BUCCI, "Experimental and Computational Analysis of Steam Condensation Phenomena for the Thermal-Hydraulics Analysis of LWRs Containments," PhD Thesis, University of Pisa (2009).
19. M. BUCCI et al., "Prediction of Transpiration Effects on Heat and Mass Transfer by Different Turbulence Models," *Nucl. Eng. Des.*, **38**, 958 (2008).
20. W. AMBROSINI et al., "Experimental and CFD Analysis on Condensation Heat Transfer in a Square Cross Section Channel," *Proc. 11th Int. Topl. Mtg. Nuclear Reactor Thermal Hydraulics (NURETH-11)*, Avignon, France, October 2–6, 2006.
21. S. MOGLIANI, "Analisi teorica e sperimentale della condensazione in presenza di gas incondensabili," Master's Thesis, University of Pisa (2005).
22. N. FORGIONE and S. PACI, "Computational Analysis of Vapor Condensation in Presence of Air in the TOSQAN Facility," *Proc. 11th Int. Topl. Mtg. Nuclear Reactor Thermal Hydraulics (NURETH-11)*, Avignon, France, October 2–6, 2006.
23. M. BUCCI, "Sviluppo di modelli di CFD per lo studio della condensazione nel sistema di contenimento di LWRs," Master's Thesis, University of Pisa (2005).
24. M. BUCCI et al., "Validation of a CFD Condensation Model Based on the Heat and Mass Transfer Analogy by TOSQAN Facility ISP47 Test," *Proc. 14th Int. Conf. Nuclear Engineering (ICONE 14)*, Miami, Florida, July 17–20 2006, ASME (2006).
25. M. BUCCI et al., "Modeling of Steam Condensation Phenomena in the Presence of Noncondensable Gases: Analysis of Separate Effect Tests in Forced, Natural and Mixed Convection," *Proc. 13th Int. Topl. Mtg. Nuclear Reactor Thermal Hydraulics (NURETH-13)*, Kanazawa City, Ishikawa Prefecture, Japan, September 27–October 2, 2009.
26. "Fluent 6.2 User Guide," FLUENT, Inc. (2003).
27. M. BUCCI et al., "Theoretical and Computational Analysis of Diffusion Phenomena in Condensing Multicomponent Mixtures," *Nucl. Eng. Des.* (2010) (submitted for publication).
28. R. TAYLOR and R. KRISTHNA, *Multicomponent Mass Transfer*, Wiley (1993).

29. J. STEFAN, "Versuche über die verdampfung," *Sber. Akad. Wiss. Wien.*, **68**, 385 (1873).
30. H. SCHLICHTING, *Boundary Layer Theory*, McGraw-Hill (1981).
31. F. P. INCROPERA, *Fundamentals of Heat Transfer*, Wiley (1965).
32. P. BAZIN and P. CASTELLI, "COPAIN: rapport d'essai," SETEX/LETS/99-85, Commissariat à l'Energie Atomique (Dec. 2003).
33. G. ACKERMAN, "Wämeübertregung und molekulare stoffübertragung in gleichen feld bei grosser temperature und partialdruckdifferenzen," *Forschft. Ver. Dt. Ing.*, **328**, 1 (1937).
34. R. J. MOFFAT, "Describing the Uncertainties in Experimental Results," *Exp. Fluid Sci.*, **1**, 3 (1988).
35. D. B. SPALDING, "A Standard Formulation of the Steady Convective Mass Transfer Problem," *Int. J. Heat and Mass Transfer*, **1**, 192 (1960).
36. J. H. LIENHARD, *A Heat Transfer Textbook*, Prentice Hall, Englewood Cliffs (1997).
37. W. AMBROSINI et al., "On Various Forms of the Heat and Mass Transfer Analogy: Discussion and Application to Condensation Experiments," *Nucl. Eng. Des.*, **236**, 1013 (2010).
38. T. H. CHILTON and A. P. COLBURN, "Evaporation of Water into a Laminar Stream of Air and Superheated Steam," *Ind. Eng. Chem.*, **26**, 373 (1934).
39. P. F. PETERSON, V. E. SCHROCK, and T. KAGEYAMA, "Diffusion Layer Theory for Turbulent Vapor Condensation with Noncondensable Gases," *J. Heat Transfer*, **115**, 998 (1993).
40. R. BIRD, W. E. STEWART, and E. N. LIGHTFOOT, *Transport Phenomena*, Wiley, New York (1960).